

Exciton-driven giant non-linear overtone signals from buckled hexagonal monolayer GaAs

Himani Mishra and Sitangshu Bhattacharya*

*Nanoscale Electro-Thermal Laboratory, Department of Electronics and Communication Engineering,
Indian Institute of Information Technology-Allahabad, Uttar Pradesh 211015, India*

I. THEORETICAL DISCUSSIONS

A. Linear spectra: $\mathbf{G}_0\mathbf{W}_0$ and Bethe-Salpeter Equation

Within the linear response many body perturbation theory (MBPT), the electron-electron (ee) interaction is both exchanged and correlated. The corresponding total self-energy is written as sum of these. The first one is the Hartree-Fock exchange self-energy $\sum_{n\mathbf{k}}^x$, and is the static one. The matrix elements of this self-energy in the plane wave basis set is diagonal and can be expressed as [1, 2]

$$\sum_{n\mathbf{k}}^x = \langle n\mathbf{k} | \sum^x | n\mathbf{k} \rangle = - \sum_m \int_{BZ} \frac{d\mathbf{q}}{(2\pi)^3} \sum_{\mathbf{G}} v(\mathbf{q} + \mathbf{G}) |\rho_{nm}(\mathbf{k}, \mathbf{q}, \mathbf{G})|^2 f_{m(\mathbf{k}-\mathbf{q})} \quad (1)$$

in which $|n\mathbf{k}\rangle$ is the momentum state of n^{th} band, \mathbf{q} are the transferred momenta, m are the number of electronic bands, f is the Fermi function and ρ is the charge density. \mathbf{G} are the G -vectors with $v(\mathbf{q} + \mathbf{G}) = \frac{4\pi}{|\mathbf{q} + \mathbf{G}|^2}$ as the three-dimensional Coulomb potential in the Fourier transformed plane.

At this level, the Hartree-Fock contribution to the ground state density functional theory (DFT) energy eigenvalues can be written as

$$E_{n\mathbf{k}}^{HF} = E_{n\mathbf{k}}^{DFT} + (\sum_{n\mathbf{k}}^x - V_{n\mathbf{k}}^{xc}) \quad (2)$$

in which $V_{n\mathbf{k}}^{xc}$ is the exchange and correlation functional at the level of time-independent local density or generalized gradient approximation, borrowed from DFT.

The second part of the electron-electron self energy is the correlation part $\sum_{n\mathbf{k}}^c(\omega)$, and is both long-range and dynamic. This can be written as

$$\langle n\mathbf{k} | \sum^{ee}(\omega) | n\mathbf{k} \rangle = i \sum_m \int_{BZ} \frac{d\mathbf{q}}{(2\pi)^3} \sum_{\mathbf{G}, \mathbf{G}'} \frac{4\pi}{|\mathbf{q} + \mathbf{G}|^2} \rho_{nm}(\mathbf{k}, \mathbf{q}, \mathbf{G}) \rho_{nm}^*(\mathbf{k}, \mathbf{q}, \mathbf{G}') \int d\omega' G_{m\mathbf{k}-\mathbf{q}}^0(\omega - \omega') \varepsilon_{\mathbf{G}\mathbf{G}'}^{-1}(\mathbf{q}, \omega') \quad (3)$$

in which $\varepsilon_{\mathbf{G}\mathbf{G}'}^{-1}$ is the microscopic dynamic dielectric function and $G_{m\mathbf{k}-\mathbf{q}}^0$ is the single-particle non-interacting Green's propagator. Note that now, the screening has entered implicitly in $\varepsilon_{\mathbf{G}\mathbf{G}'}^{-1}$. Beacuse of the presence of several complex branch cuts arising while calculating the frequency integral involving this $\varepsilon_{\mathbf{G}\mathbf{G}'}^{-1}$, the enrire computation process becomes extremely expensive. What is done then is to replace $\varepsilon_{\mathbf{G}\mathbf{G}'}^{-1}$ (See Eqn. (3)) with an effective dielectric function model with single pole (See Eqn. (6)). This is known as the “plasmon-pole model” [3].

First the screening (W) is evaluated at the level of random phase approximation (RPA, i.e., using Hartree-kernel) using the Dyson-like susceptibility relation

$$\chi_{\mathbf{G}, \mathbf{G}'}(\mathbf{q}, \omega) = \chi_{\mathbf{G}, \mathbf{G}'}^0(\mathbf{q}, \omega) + \sum_{\mathbf{G}_1, \mathbf{G}_2} \chi_{\mathbf{G}, \mathbf{G}_1}^0(\mathbf{q}, \omega) [v_{\mathbf{G}_1}(\mathbf{q}, \omega) \delta_{\mathbf{G}_1, \mathbf{G}_2}] \chi_{\mathbf{G}_2, \mathbf{G}'}(\mathbf{q}, \omega) \quad (4)$$

from which the RPA dielectric function is evaluated as

$$\varepsilon_{\mathbf{G}, \mathbf{G}'}^{-1}(\mathbf{q}, \omega) = \delta_{\mathbf{G}, \mathbf{G}'} + v_{\mathbf{G}}(\mathbf{q}) \chi_{\mathbf{G}, \mathbf{G}'}(\mathbf{q}, \omega) \quad (5)$$

Plasmon-Pole approximation [3] is now used to replace this $\varepsilon_{\mathbf{G}\mathbf{G}'}^{-1}$ with a single pole function of the form

$$\varepsilon_{\mathbf{G}, \mathbf{G}'}^{-1}(\mathbf{q}, \omega) \sim \delta_{\mathbf{G}, \mathbf{G}'} + R_{\mathbf{G}, \mathbf{G}'}(\mathbf{q}) \left\{ \frac{1}{[\omega - \Omega_{\mathbf{G}, \mathbf{G}'}(\mathbf{q}) + i0^+]} - \frac{1}{[\omega + \Omega_{\mathbf{G}, \mathbf{G}'}(\mathbf{q}) + i0^+]} \right\} \quad (6)$$

The parameters $R_{\mathbf{G}, \mathbf{G}'}(\mathbf{q})$ and $\Omega_{\mathbf{G}, \mathbf{G}'}(\mathbf{q})$ are generally obtained by fitting after calculating the RPA dielectric matrix at two given frequencies. The MBPT package YAMBO [4] calculates the dielectric function at $\omega=0$ and at a user defined

* Corresponding Author's Email: sitangshu@iiita.ac.in

frequency. In our calculation, we used 27 eV to be this frequency. We checked how $\varepsilon_{\mathbf{G}\mathbf{G}'}^{-1}$ changes by increasing this until it converged at 27 eV. The local field effect was employed along the in-plane periodic direction using a response block size with a cut-off of 7 Ry.

The total self-energy is thus $\langle n\mathbf{k} | \sum^{ee} | n\mathbf{k} \rangle + \langle n\mathbf{k} | \sum^x | n\mathbf{k} \rangle$ leading to the quasi-particle (QP) energy at this level (See Eqn.(2) above) as

$$E_{n\mathbf{k}}^{QP} = E_{n\mathbf{k}}^{DFT} + Z_{n\mathbf{k}} \Re [\langle \psi_{n\mathbf{k}} | \langle n\mathbf{k} | \sum^{ee} | n\mathbf{k} \rangle + \langle n\mathbf{k} | \sum^x | n\mathbf{k} \rangle - V_{xc} | \psi_{n\mathbf{k}} \rangle] \quad (7)$$

The QP lifetimes are the reciprocal of the imaginary part of $\langle n\mathbf{k} | \sum^{ee} | n\mathbf{k} \rangle + \langle n\mathbf{k} | \sum^x | n\mathbf{k} \rangle$. The QP energies in Eqn. (7) are evaluated from the first-order Taylor's series expansion of the total self-energy around the DFT Kohn-Sham eigen-energies [5]. This factor

$$Z_{n\mathbf{k}} = \left[1 - \frac{d \sum_{n\mathbf{k}}(\omega)}{d\omega} \Big|_{\omega=E_{n\mathbf{k}}} \right]^{-1} \quad (8)$$

with $0 \leq Z_{n\mathbf{k}} \leq 1$ is then the QP renormalized weight factor. Values of Z very close to 1 signifies a pure QP state. The corresponding spectral function

$$A_{n,\mathbf{k}}(\omega, T) = \frac{1}{\pi} \frac{\left| \Im \sum^{x+ee}(\omega) \right|}{\left[\omega - E_{n\mathbf{k}}^{DFT} - \Re \sum^{x+ee}(\omega) \right]^2 + \left[\Im \sum^{x+ee}(\omega) \right]^2} \quad (9)$$

is Lorentzian and the spreading (full-width at half maximum, FWHM) defines the strength of the correlated interaction. A sharp spectral function defines a less correlated interaction, while a dwarf and spread defines a strong interaction. In reduced geometries, like in our case with ML GaAs, the divergence of the Coulomb potential integrals at small \mathbf{q} appearing in the exchange as well as in dynamic self energies are problematic. To correct this, a random integration method [6] was applied which assumes a smooth momenta integrand function (only for oscillators and occupation numbers) about \mathbf{q} in each region of the Brillouin zone (BZ) without changing the potential itself. In the spirit of Eqns. (1 and 3) and [6] we describe this method as follows: The diagonal matrix element of the exchange self-energy following this assumption can be written in the form

$$\left\langle n\mathbf{k} \left| \sum^x(\mathbf{r}_1, \mathbf{r}_2) \right| n\mathbf{k} \right\rangle \approx \sum_{\mathbf{q}_i} \sum_{\mathbf{G}} F(\mathbf{q}_i, \mathbf{G}) \int_{small\ BZ(\mathbf{q}_i)} d^3\mathbf{q} \frac{4\pi}{|\mathbf{q} + \mathbf{G}|^2} \quad (10)$$

This integral is evaluated using a numerical Monte Carlo method which resolves the $\mathbf{q} \rightarrow 0$ divergence as the three dimensional \mathbf{q} integration forbids this to happen. In addition, the integral pre-factor is also regular when $\mathbf{q}_i \rightarrow 0$. 10^6 random points were incorporated in our calculation in order to evaluate the Coulomb integrals with a \mathbf{G} -vector cut-off of 3 Ry. The numerical integral was defined within a box-structure extending 30 Å on either side of the ML GaAs. This truncated the Coulombic potential between the repeated images and a faster convergence was achieved.

Excitonic affairs are governed by a two-particle (electron and hole) Dyson-like equation of motion. In a ladder-approximation representation [1],

$$\mathcal{L}(12; 1'2') = \mathcal{L}_0(12; 1'2') + \int d(3456) \mathcal{L}_0(14; 1'3) K(35; 46) \mathcal{L}(62; 52') \quad (11)$$

in which $\mathcal{L}(12; 1'2')$ and $\mathcal{L}_0(12; 1'2')$ are the interacting and non-interacting two-particle Green's propagator respectively. The variable “(1)” (and similar others) is a short hand notation for the spatial, spin and four time (two creation and two annihilation) coordinates: $(1) \equiv (r_1, \sigma_1, t_1)$ respectively. In case of occupied (v) and unoccupied (c) states, \mathcal{L}_0 in Fourier transform plane has the form

$$\mathcal{L}_0^{vcv'c'}(\omega) = \frac{1}{\omega - (E_c^{DFT} - E_v^{DFT}) + i\eta} \delta_{cc'} \delta_{vv'} \quad (12)$$

Note here that the four time variables are now decomposed in a single frequency in the ω plane.

The kernel $K_{vc\mathbf{k}v'c'\mathbf{k}'}$ is a functional static quantity and is the sum of a bare exchange Coulomb repulsion and statically screened Coulomb attraction between the electron and hole. The later is represented as

$$W(v\mathbf{c}\mathbf{k}; v'c'\mathbf{k}_1) = \frac{1}{\Omega} \sum_{\mathbf{G}\mathbf{G}'} v(\mathbf{q} + \mathbf{G}') \epsilon_{\mathbf{G}\mathbf{G}'}^{-1}(\mathbf{q}) \langle v'\mathbf{k}_1 | e^{-i(\mathbf{q}+\mathbf{G}')\cdot\mathbf{r}} | v\mathbf{k} \rangle \langle c\mathbf{k} | e^{i(\mathbf{q}+\mathbf{G}')\cdot\mathbf{r}} | c'\mathbf{k}_1 \rangle \delta_{\mathbf{q}, \mathbf{k}-\mathbf{k}_1} \quad (13)$$

while the former is

$$V(v\mathbf{c}\mathbf{k}; v'c'\mathbf{k}_1) = \frac{1}{\Omega} \sum_{\mathbf{G} \neq 0} v(\mathbf{G}) \langle v'\mathbf{k}_1 | e^{-i\mathbf{G}\cdot\mathbf{r}} | c'\mathbf{k} \rangle \langle c\mathbf{k} | e^{i\mathbf{G}\cdot\mathbf{r}} | v\mathbf{k} \rangle \quad (14)$$

where Ω in this case is the cell volume. K is thus defined as $K_{v\mathbf{c}\mathbf{k};v'\mathbf{c}'\mathbf{k}'} = \langle v\mathbf{c}\mathbf{k} | W - 2V | v'\mathbf{c}'\mathbf{k}' \rangle$. It is in this statically screened kernel W in which the G_0W_0 QP energies are included to get the correct transition energies. Note that in order to obtain a solvable BSE [7], W is approximated to be a static, which can be borrowed from the preceding dynamic screening calculations in G_0W_0 simply by putting $\omega=0$.

Assuming that the off-diagonal elements in the self-energies are small, so as to make the total Hamiltonian a hermitian that would also guarantee orthogonal QP states, the exciton equation of motion (i.e., the BSE) is

$$\left(E_{\mathbf{c}\mathbf{k}}^{QP} - E_{v\mathbf{k}}^{QP}\right) A_{v\mathbf{c}\mathbf{k}}^s + \sum_{v'\mathbf{c}'\mathbf{k}'} \langle v\mathbf{c}\mathbf{k} | K_{vv',v'\mathbf{c}'\mathbf{k}'} | v'\mathbf{c}'\mathbf{k}' \rangle A_{v\mathbf{c}\mathbf{k}}^s = E_X^S A_{v\mathbf{c}\mathbf{k}}^s \quad (15)$$

in which S is each exciton (i.e., a pair state with a distinct principal quantum number and momentum wave-vector difference between v and c), E_X is the excitonic energy that is obtained by diagonalizing this hamiltonian and $A_{v\mathbf{c}\mathbf{k}}^s$ is the excitonic amplitude in the electron-hole basis and contains the light polarization direction. As the momentum wave-vector difference is zero for vertical transitions, which is conserved by photon momentum, therefore excitons with vertical transitions (bright excitons) are only detectable. The resonant Green's propagator is then

$$\mathcal{L}_{vc,v'\mathbf{c}'}(\omega) = \sum_S \frac{A_{v\mathbf{c}\mathbf{k}}^S A_{v\mathbf{c}\mathbf{k}}^{S*}}{\omega - E_X + i\eta} \quad (16)$$

The numerator can be obtained via residue theorem and signifies the exciton oscillator strength. The macroscopic dielectric function (i.e., the absorption spectra) is thus evaluated in limit of long wavelength $\mathbf{q}_S \rightarrow 0$

$$\varepsilon_M(\omega) = -\left(\frac{8\pi}{\Omega}\right) \sum_S |A_{v\mathbf{c}\mathbf{k}}^S|^2 \Im \left(\frac{1}{\omega - E_X + i\eta} \right) \quad (17)$$

This is also the linear response function $\chi_{ij}^{(1)}(\omega)$.

In order to analyse if the exciton is ‘‘Frenkel’’ or ‘‘Wannier’’-type, the exciton wave-function is needed. This can be written as

$$|\Phi^S(\mathbf{r}_e, \mathbf{r}_h)\rangle = \sum_{v\mathbf{c}\mathbf{k}} A_{v\mathbf{c}\mathbf{k}}^S \phi_{v\mathbf{k}}(\mathbf{r}_e) \phi_{c\mathbf{k}}(\mathbf{r}_h) \quad (18)$$

in which \mathbf{r}_e and \mathbf{r}_h are the electron and hole coordinates in real-space. We note that the evaluation of this wave-function would require six-coordinates. Thus, we fix the hole position on the top of As atom and obtain the projection $|\Phi^S[(0,0,0), (0,0,0)]|^2$ on the x - y plane. This has been exhibited as inset of Fig. 2 in the main text.

B. Non linear spectra: Time-dependent Schrödinger's equation

The time-development of occupied states $|\nu_{n\mathbf{k}}\rangle$ can be obtained from a time-dependent (TD) Schrödinger's equation as [8]

$$i\hbar \frac{d}{dt} |\nu_{n\mathbf{k}}\rangle = \left[\mathcal{H}_{\mathbf{k}}^{system} + i\mathcal{E}(t) \cdot \tilde{\partial}_{\mathbf{k}} \right] |\nu_{n\mathbf{k}}\rangle \quad (19)$$

in which $\mathcal{H}_{\mathbf{k}}^{system}$ is the system Hamiltonian and $\mathcal{E}(t) \cdot \tilde{\partial}_{\mathbf{k}}$ is the coupling of the electrons with the external field. If the system is periodic, the Born-von Kármán periodic boundary condition impose the operator $\tilde{\partial}_{\mathbf{k}} \equiv \frac{\partial}{\partial \mathbf{k}}$. The solutions to this equation are then gauge invariant under unitary transformations of the Bloch state $|k\rangle$.

Instead of a perturbative way (i.e., in the Fourier transformed domain), Eqn.(19) is solved directly in the real-time (RT) domain. The reasons are straightforward. A perturbative scheme is always computationally very expensive whereas in RT, the many-body effects can be efficiently added in the hamiltonian.

In order to find the macroscopic polarization, we follow the modern theory of polarization by King-Smith and Vanderbilt [9]. These authors argued that the Berry's phase change generated by a closed path in \mathbf{k} -space correctly defines the macroscopic polarization of a periodic system. When the states $|\nu_{n\mathbf{k}}\rangle$ are known, the in-plane macroscopic polarization along the lattice vector a can then be evaluated from

$$\mathcal{P}_{\parallel} = -\frac{eg_s}{2\pi\Omega} \frac{|a|}{N_{\mathbf{k}_{\perp}}} \sum_{\mathbf{k}_{\perp}} \Im \log \prod_{\mathbf{k}_{\parallel}}^{N_{\mathbf{k}_{\parallel}}-1} \det S(\mathbf{k}, \mathbf{k} + \mathbf{q}_{\parallel}) \quad (20)$$

in which e is the electronic charge, g_s is the spin degeneracy, Ω is the cell volume, $S(\mathbf{k}, \mathbf{k} + \mathbf{q}_{\parallel})$ is the overlap matrix between the the states $|\nu_{n\mathbf{k}}\rangle$ and $|\nu_{m\mathbf{k}+\mathbf{q}_{\parallel}}\rangle$, $N_{\mathbf{k}_{\parallel}}$ and $N_{\mathbf{k}_{\perp}}$ are the respective in-plane and out-of plane \mathbf{k} -points to the polarization direction with $q_{\parallel} = \frac{2\pi}{N_{\mathbf{k}_{\parallel}}}$.

The system hamiltonian in Eqn. (19) can now be constructed as follows: In the independent-particle approximation (IPA), the energy eigenvalues are simply evaluated from the Kohn-Sham DFT hamiltonian

$$\mathcal{H}_k^{system} = \mathcal{H}_k^{DFT} \quad (21)$$

Next, the G_0W_0 corrections can be added to this IPA hamiltonian as either by a scissor operator

$$\mathcal{H}_{\mathbf{k}}^{system} = \mathcal{H}_k^{DFT} + \Delta\mathcal{H}^{scissor} = \mathcal{H}_k^{DFT} + \sum_{n\mathbf{k}} \Delta_{n\mathbf{k}} |v_{n\mathbf{k}}^0\rangle \langle v_{n\mathbf{k}}^0| \quad (22)$$

or directly by $\Delta_{n\mathbf{k}} = E_{n\mathbf{k}}^{G_0W_0} - E_{n\mathbf{k}}^{DFT}$ from an *ab-initio* computation.

The next hierarchy is the TD-DFT, where the system hamiltonian is [10]

$$\mathcal{H}_{\mathbf{k}}^{system} = \mathcal{H}_{\mathbf{k}}^{DFT} + V_H [\Delta\rho(r, t)] + V_{xc}(r) [\Delta\rho(r, t)] \quad (23)$$

in which V_H is the self-consistent Hartree potential, and V_{xc} is the exchange-correlation potential at the level of Kohn-Sham DFT, now calculated quasi-statically within LDA or GGA. These two potentials are dependent on the time-varying electronic density $\rho(r, t)$. Random phase approximation is the condition when V_{xc} is neglected in the system hamiltonian. The change $\Delta\rho(r, t) = \rho(r, t) - \rho(r, 0)$ is the electronic density variation and is responsible for the local-field effects due to the inhomogeneities in the system.

The next level of hierarchy is the incorporation of scissor-corrected screen-exchange (SEX) interaction in the hamiltonian. This is usually known as TD-BSE [8]

$$\mathcal{H}_{\mathbf{k}}^{system} = \mathcal{H}_{\mathbf{k}}^{DFT} + \Delta\mathcal{H}_{\mathbf{k}}^{scissor} + V_H [\Delta\rho(r, t)] + \sum_{SEX} [\Delta\gamma] \quad (24)$$

in which $\Delta\gamma(r, r', t) = \gamma(r, r', t) - \gamma(r, r', 0)$ is the density fluctuation matrix induced by the external field. The self-energy \sum_{SEX} is the convolution between the statically screened interaction W and $\Delta\gamma(r, r', t)$.

The equation of motion (Eqn.(18)) is now numerically solved for $|\nu_{n\mathbf{k}}\rangle$ using the following algorithm developed by Crank and Nicholson [11] for both Hermitian and non-Hermitian type hamiltonians

$$|v_{n\mathbf{k}}(t + \Delta t)\rangle = \frac{I - i(\Delta t/2) \mathcal{H}_{\mathbf{k}}^{system}(t)}{I + i(\Delta t/2) \mathcal{H}_{\mathbf{k}}^{system}(t)} |v_{n\mathbf{k}}(t)\rangle \quad (25)$$

in which I is the identity element. The operation is strictly unitary for any value of time-step Δt .

It turns out that if the applied field is a Dirac delta-type, the Fourier transformed responses can be evaluated at all frequencies. In case of a low intensity, one can show that Eqn. (19) with BSE correction is equivalent to the Eqn. (15) [12]. These are numerically shown in Fig. S10(a). The extraction of the non-linear response function is a post-processing computation. We follow Attacalite *et. al.* [8] for this methodology. As shown in Fig. S10(c), the sudden switching of a monochromatic $\mathcal{E}(t)$ induces spurious fluctuations at the initial stage. In order to calculate the $\mathcal{P}(t)$ from a clean signal, we add a dephasing time-constant of 7 fs. This would essentially mean that after 5 time-constants (~ 32 fs) these spurious fluctuations are sufficiently cleared out from $\mathcal{P}(t)$ and the non-linear responses can be obtained between this time and the total simulation time (~ 55 fs). There are two approaches by which non-linear χ can be evaluated. Either, the field may be applied in a quasi-static way, so that the spurious fluctuations does not appear. However calculating \mathcal{P} in this way takes a long time to simulate [8]. The other way is to use the previous sudden approximation and change the following Fourier series into a system of linear equations. The polarization Fourier series is

$$\mathcal{P}(t) = \sum_{n=-\infty}^{n=\infty} p_n e^{-i\omega_n t} \quad (26)$$

We follow [8] and truncate this series to an order \mathcal{S} larger than the response we are interested to calculate. With a laser frequency ω_L , we find the time-period T_L and within this we sample the signal to $2\mathcal{S} + 1$ values. Eqn. (26) can now be transformed in a system of linear equation

$$\mathcal{F}_{lin} p_n^\alpha = \mathcal{P}_i^\alpha \quad (27)$$

in which α is the polarization direction. By Fourier inversion of the $(2\mathcal{S} + 1) \times (2\mathcal{S} + 1)$ matrix (done on sampled times t_i) ($\mathcal{F}_{lin} \equiv e^{-i\omega_n t_i}$), each component p_n^α of the coefficients p_n can be obtained.

II. SUPPORTING CONVERGENCE FIGURES AND ADDED GRAPHICAL INFORMATION

A. Monolayer hexagonal buckled GaAs structure after energy minimization

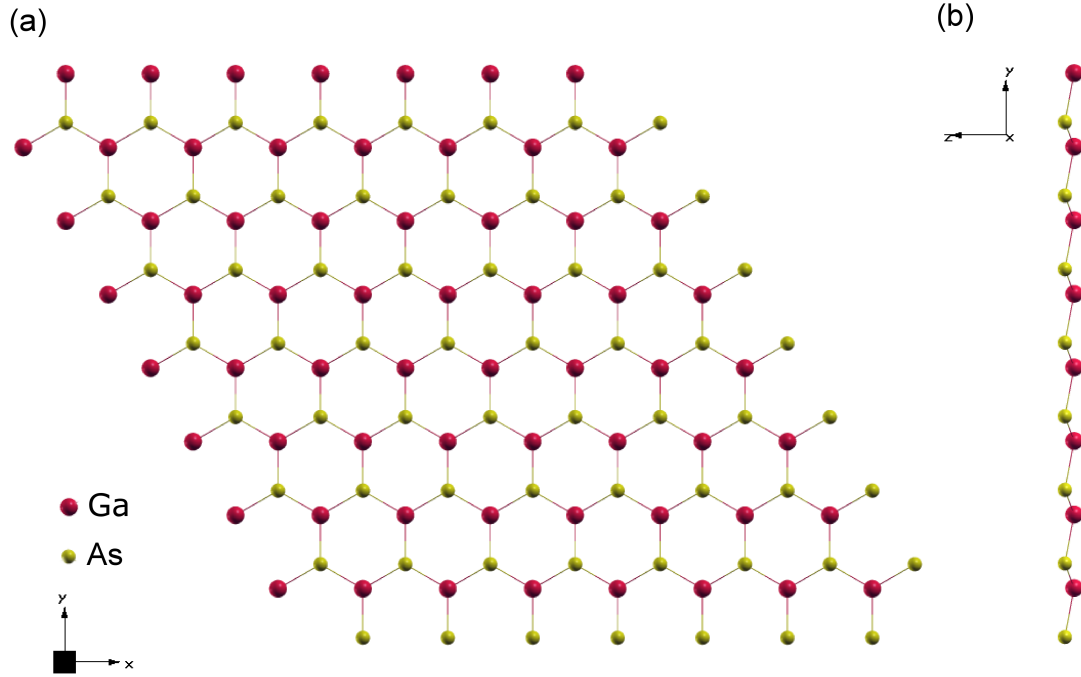


FIG. S1. (a) In-plane monolayer GaAs exhibiting a hexagonal structure with in-plane lattice constant of 4.05 Å. (b) The buckling height along the out-of-plane (z-direction) is found to be 0.58 Å.

B. Kinetic cut-off convergences

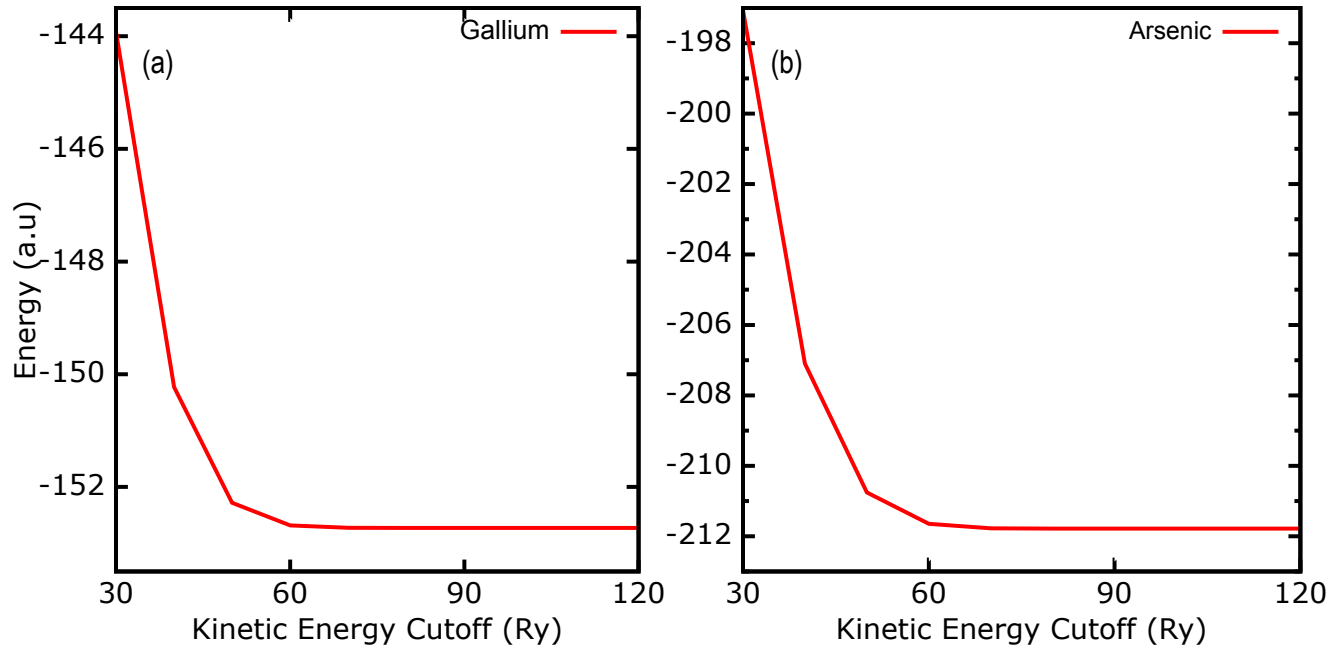


FIG. S2. Total energy minimization as function of kinetic energy cut-off using a norm-conserving fully relativistic pseudo-potential of (a) Gallium and (b) Arsenic. We see that the energy settles at 120 Ry in both cases. We therefore choose 120 Ry in all our subsequent computations.

C. k -point sampling convergences in the absence of spin-orbit coupling case

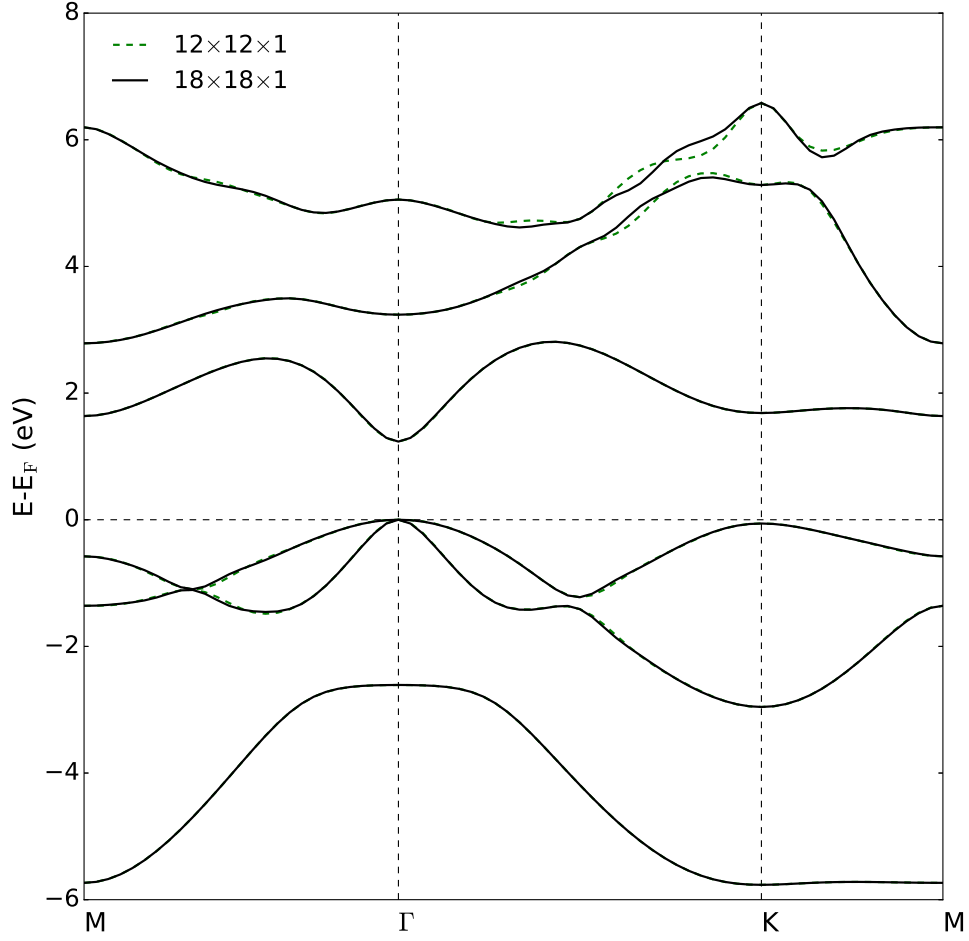


FIG. S3. Ground state electron energy dispersion in ML buckled GaAs using kinetic energy cut-of 120 Ry and using a norm-conserving fully relativistic pseudo-potential in absence of spin-orbit coupling for k -point sampling of $12 \times 12 \times 1$ and $18 \times 18 \times 1$. We see that the sampling to $18 \times 18 \times 1$ does not improve energies even within meV region, and therefore in all our subsequent DFT analyses, we use $12 \times 12 \times 1$ sampling. E_F is the Fermi energy and the top of the valence band is set to zero energy scale.

D. k -point sampling convergences in the presence of spin-orbit coupling case

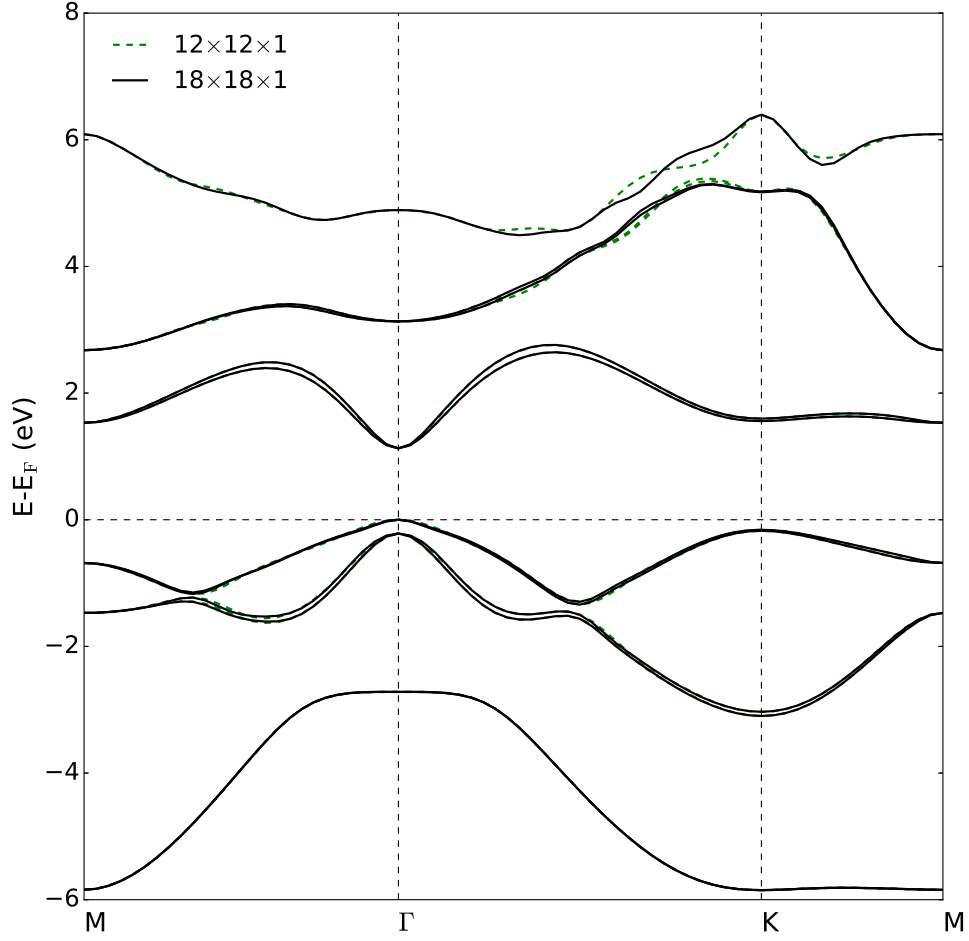


FIG. S4. Ground state electron energy dispersion in ML buckled GaAs using kinetic energy cut-of 120 Ry and using a norm-conserving fully relativistic pseudo-potential in presence of spin-orbit coupling for k -point sampling of $12 \times 12 \times 1$ and $18 \times 18 \times 1$. We see that the influence of spin-orbit coupling demonstrate a “Zeeman”-like splitting in the top of the valence band at Γ . Dense sampling to $18 \times 18 \times 1$ does not improve energies in the conduction and valence bands vicinity to 0-line. Therefore in all our subsequent DFT analyses, we have used $12 \times 12 \times 1$ sampling. E_F is the Fermi energy and the top of the valence band is set to zero energy scale.

E. Energy band structure comparison in the presence and absence of spin-orbit coupling

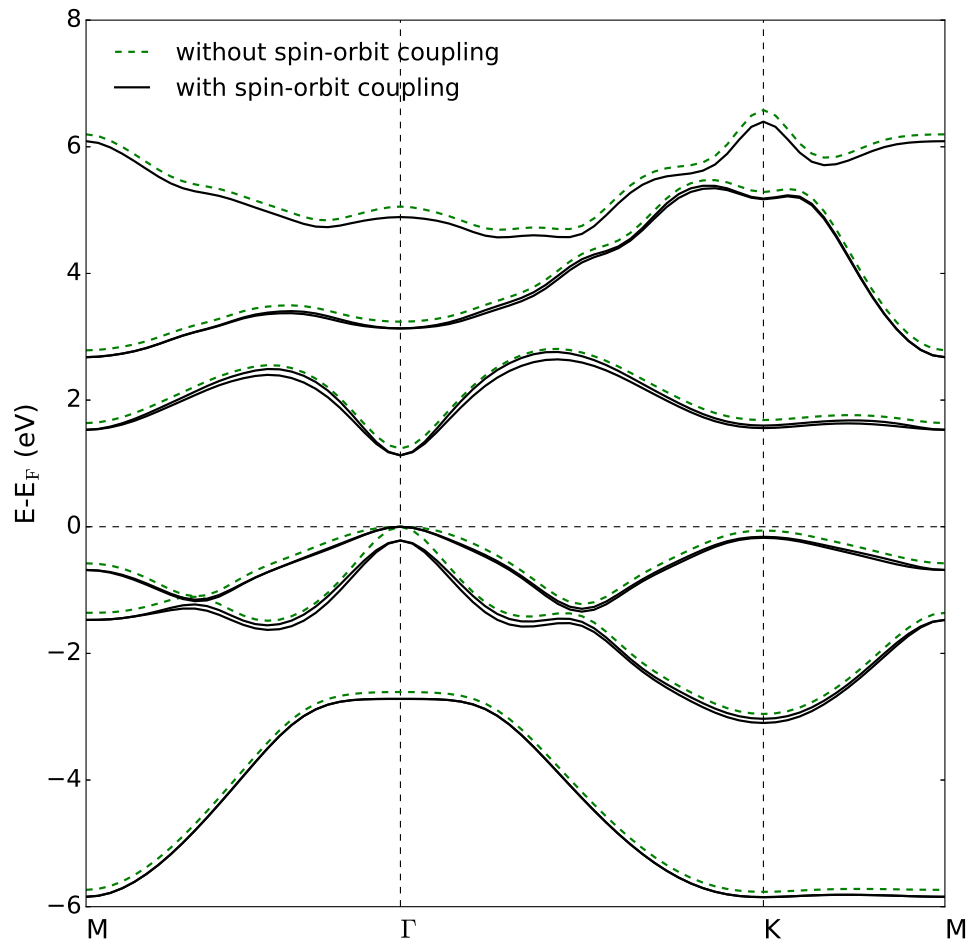


FIG. S5. Ground state electron energy dispersion in ML buckled GaAs in the presence and absence of spin-orbit coupling. We see that the influence of spin-orbit coupling demonstrate a “Zeeman”-like splitting in the top of the valence band at Γ . E_F is the Fermi energy and the top of the valence band is set to zero energy scale.

F. Orbital contributions to the ground state band structure

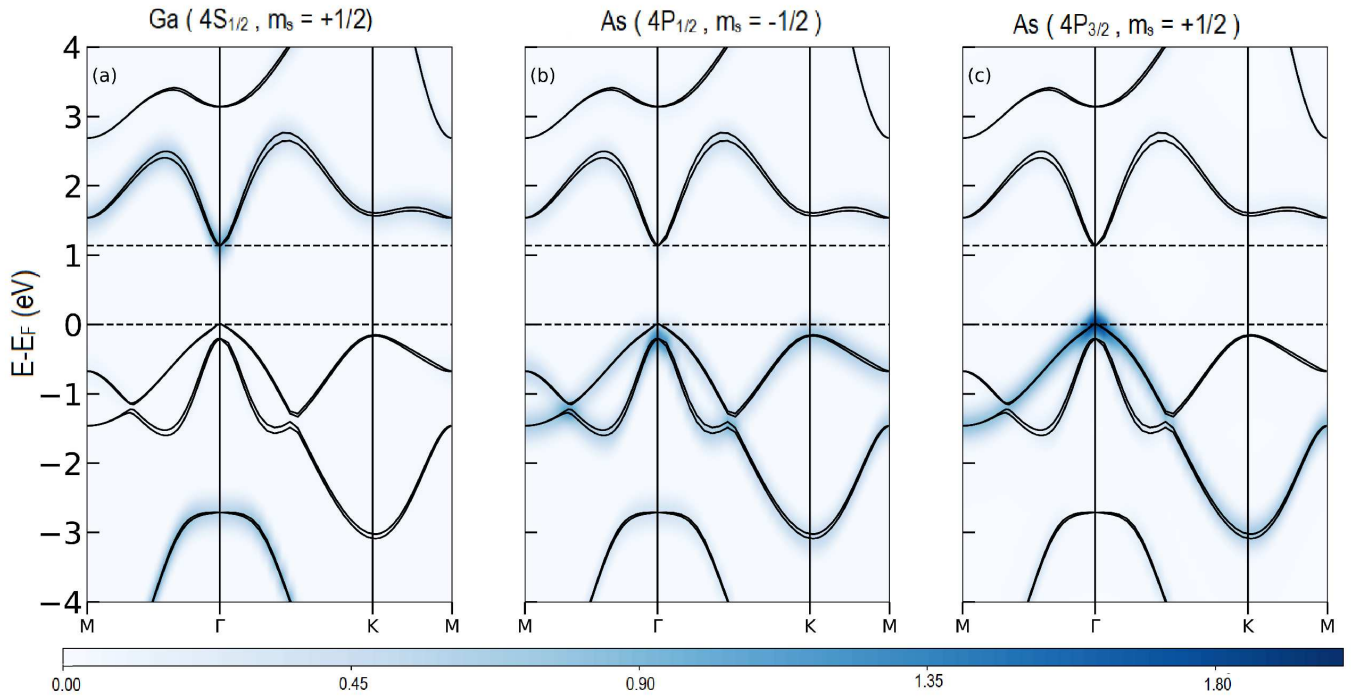


FIG. S6. Ground state electron energy dispersion in ML buckled GaAs demonstrating that at Γ , the major orbital contributions are from (a) Ga $4S_{1/2}$ (spin quantum number, $m_s = +1/2$) at the bottom of the conduction band, (b) $4P_{1/2}$ ($m_s = -1/2$) at the next highest of the valence band and (c) $4P_{3/2}$ ($m_s = +1/2$) at the highest of the valence band. The contours have been plotted on the same scale. E_F is the Fermi energy and the top of the valence band is set to zero energy scale.

G. Phonon dispersion convergences

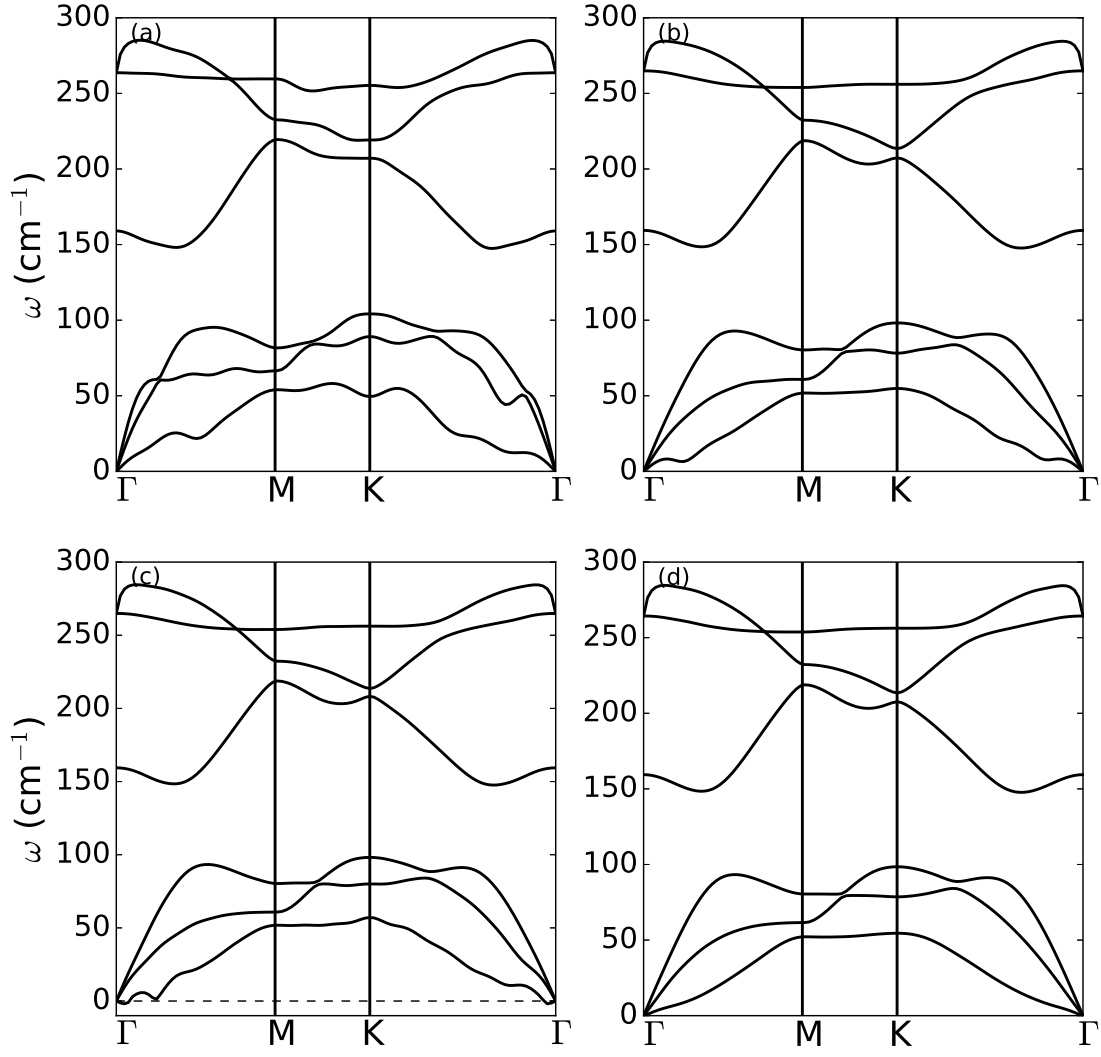


FIG. S7. Phonon dispersion curves showing the convergences using (a) $12 \times 12 \times 1$ phonon grid and a rigid self-consistent error threshold below 10^{-12} Ry, (b) $14 \times 14 \times 1$ phonon grid and a rigid self-consistent error threshold below 10^{-14} Ry, (c) $18 \times 18 \times 1$ phonon grid and a rigid self-consistent error threshold below 10^{-16} (soft-modes are seen in the vicinity of Γ along Γ - \mathbf{M} route) Ry and (d) $18 \times 18 \times 1$ phonon grid and a rigid self-consistent error threshold below 10^{-18} Ry. Clearly, (d) shows a converged result with no soft-modes for the geometry in Fig. S1.

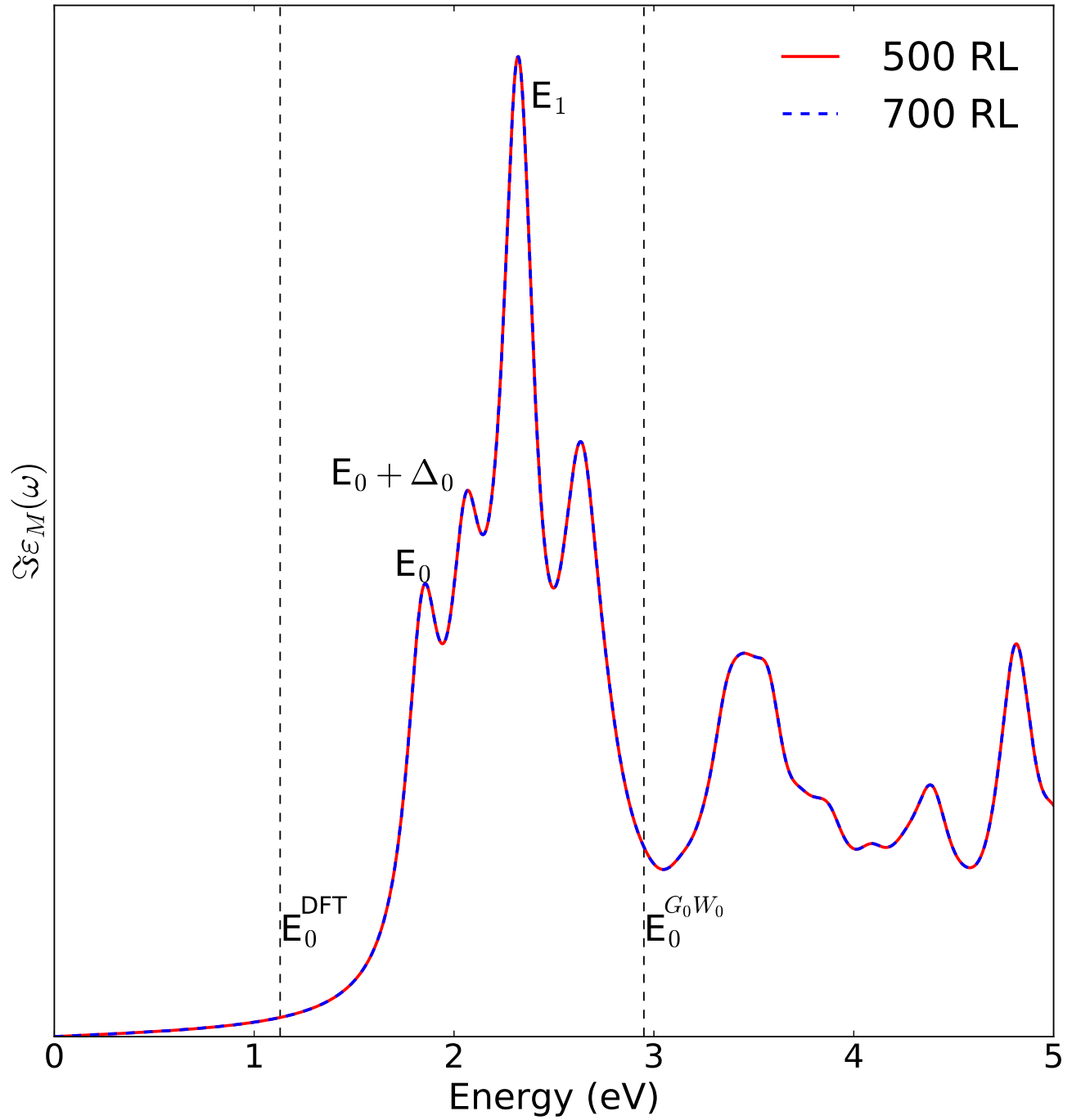


FIG. S8. Comparison between the absorption spectra for two different values of the response block size used in calculation of local field effects (LFEs). As optical spectra are very sensitive to the k -point sampling, we perform all our static and time-dependent spectra on $72 \times 72 \times 1$ k -point grid. Here the cut-off energies are in the unit of reciprocal lattice (RL) vectors. We see that the convergence is achieved for both 500 RL (~ 7 Ry) and 700 RL (~ 9 Ry).

I. BSE absorption spectra convergence with respect to transition bands

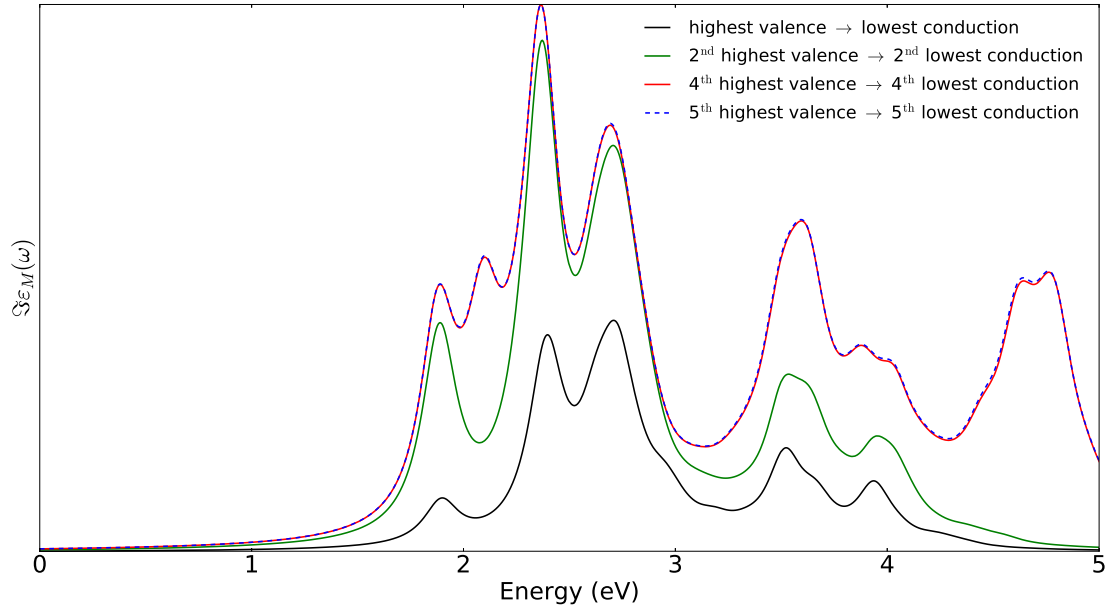


FIG. S9. Convergence of absorption spectra with respect to the number of conduction and valence bands. The local field effect cut-off of 7 Ry is used from the preceding Fig. S8. As optical spectra are very sensitive to the k -point sampling, we perform all our static and time-dependent spectra on $72 \times 72 \times 1$ k -point grid. An excellent convergence is shown using top 5 valence and lowest 5 conduction bands.

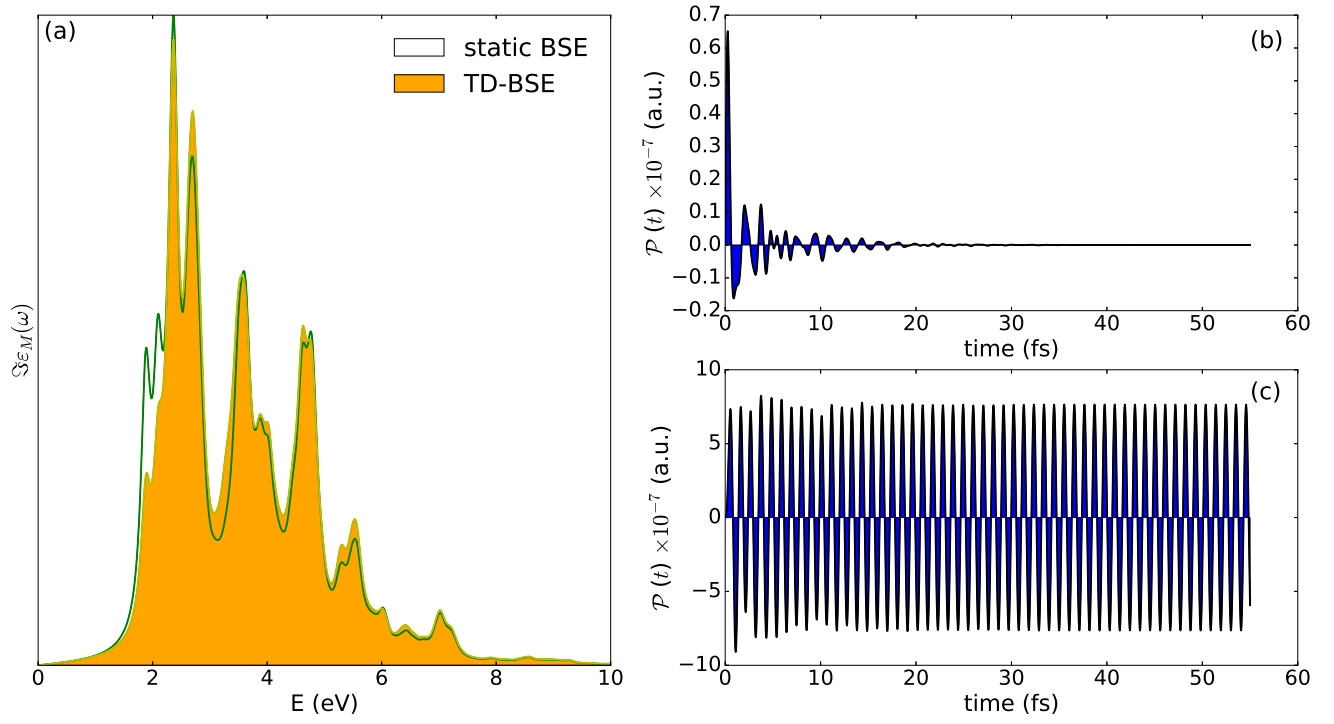


FIG. S10. (a) Comparison between the absorption spectra of ML buckled GaAs calculated with real-time approach (Eqns. (19) and (24)) and direct (static) BSE (Eqn. (15)). A scissor is added in both the cases to mimic G_0W_0 corrections. The real-time spectra is obtained by applying a delta-like electric field of intensity 500 KWcm^{-2} . The corresponding induced electric polarization is shown in (b). (c) Induced polarization along crystal b -axis in the presence of a quasi-monochromatic electric field along the a -axis. The initial sudden response can be seen in which vanishes almost at 32 fs. All of these computations were performed on $72 \times 72 \times 1$ k -point grid.

K. SHG spectra using real-time approach

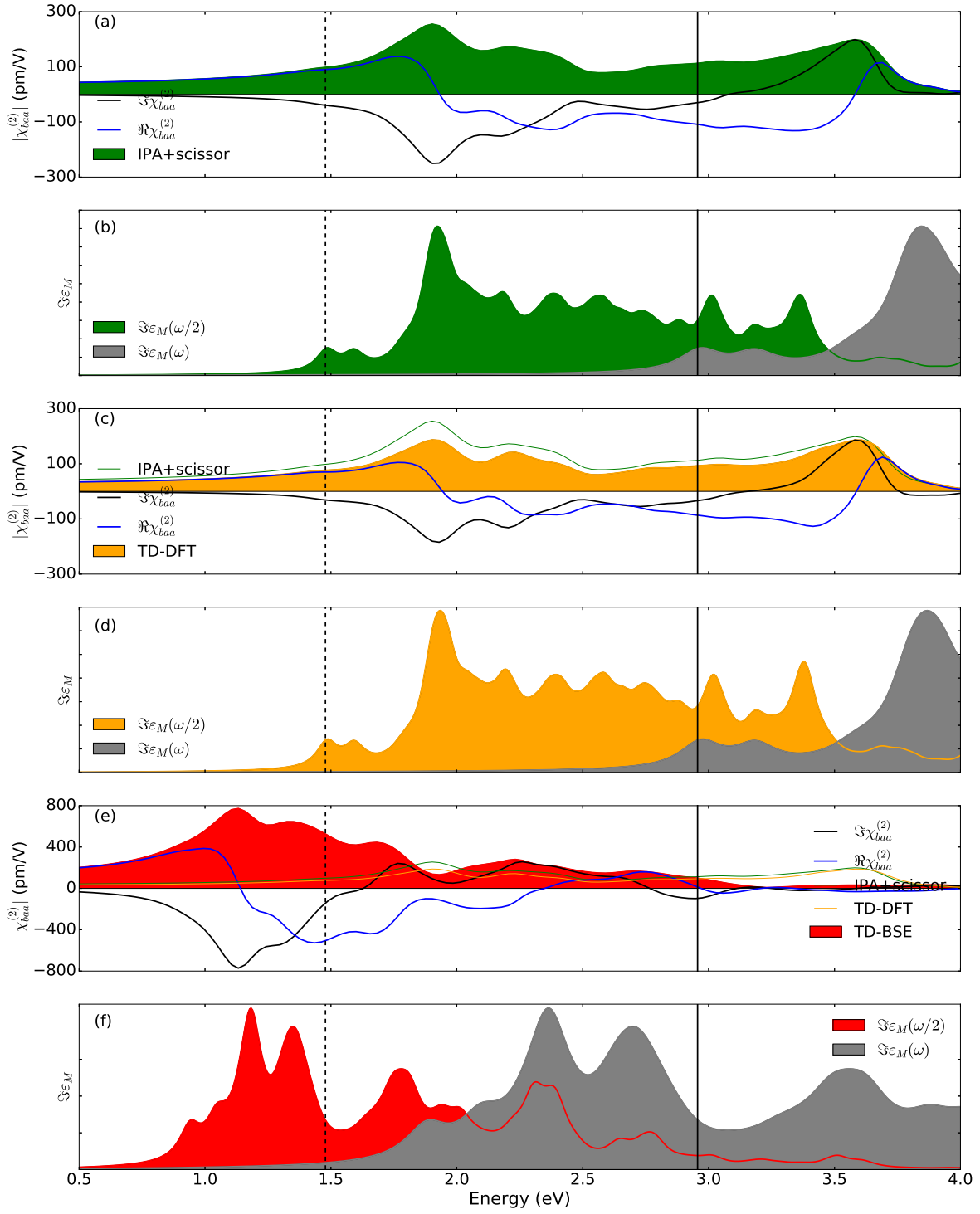


FIG. S11. Non linear SHG spectra of ML buckled GaAs as function of laser frequencies. (a), (c) and (e) are the SHG computed using IPA+scissor, TD-DFT and TD-BSE level of theory respectively (all are respective absolute values). (b), (d) and (f) shows the absorption spectra computed at ω and $\omega/2$ under the IPA+scissor, TD-DFT and TD-BSE level of theory respectively. The solid and dashed vertical lines are for the ω and $\omega/2$ gaps. The imaginary and real parts for each of the theory are also presented. From the imaginary part, one can see that $\Im \chi_{baa}^{(2)}$ goes to zero below half of the band-gap in all the cases. All of these computations were performed on $72 \times 72 \times 1$ k -point grid.

L. THG spectra using real-time approach

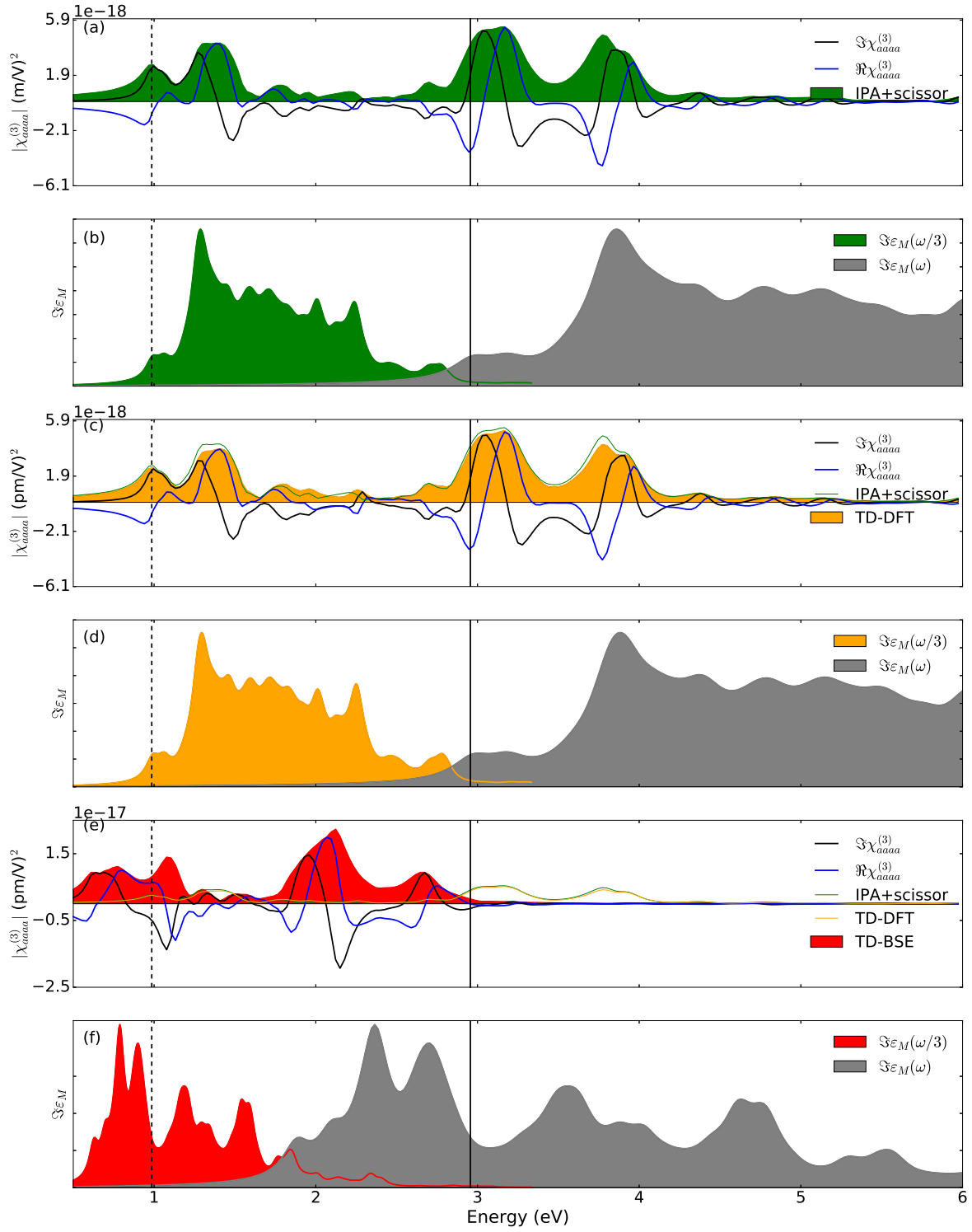


FIG. S12. Non linear THG spectra of ML buckled GaAs as function of laser frequencies. (a), (c) and (e) are the THG computed using IPA+scissor, TD-DFT and TD-BSE level of theory respectively (all are respective absolute values). (b), (d) and (f) shows the absorption spectra computed at ω and $\omega/3$ under the IPA+scissor, TD-DFT and TD-BSE level of theory respectively. The solid and dashed vertical lines are for the ω and $\omega/3$ gaps. The imaginary and real parts for each of the theory are also presented. From the imaginary part, one can see that $\Im\chi_{aaaa}^{(3)}$ goes to zero below one-third of the band-gap in all the cases. All of these computations were performed on $72 \times 72 \times 1$ k -point grid.

-
- [1] M. Rohlfing and S. G. Louie, Phys. Rev. B **62**, 4927 (2005).
 - [2] A. L. Fetter and J. D. Walecka, *Quantum Theory of Many-Particle Systems*, 1st ed. (Dover Publications Inc., Mineola, New York, United States of America, 2013).
 - [3] R. W. Godby and R. J. Needs, Phys. Rev. Lett. **62**, 1169 (1989).
 - [4] D. Sangalli, A. Ferretti, H. Miranda, C. Attaccalite, I. Marri, E. Cannuccia, P. Melo, M. Marsili, F. Paleari, A. Marrazzo, G. Prandini, P. Bonfà, M. O. Atambo, F. Affinito, M. Palummo, A. Molina-Sánchez, C. Hogan, M. Grüning, D. Varsano, and A. Marini, J. Phys.: Condens. Matter **31**, 325902 (2019).
 - [5] G. D. Mahan, *Many-Particle Physics*, 3rd ed. (Springer International Edition, New York, United States of America, 2014).
 - [6] C. A. Rozzi, D. Varsano, A. Marini, E. K. U. Gross, and A. Rubio, Phys. Rev. B **73**, 205119 (2006).
 - [7] A. Marini and R. D. Sole, Phys. Rev. Lett. **91**, 176402 (2003).
 - [8] C. Attaccalite and M. Grüning, Phys. Rev. B **88**, 235113 (2013).
 - [9] R. D. King-Smith and D. Vanderbilt, Phys. Rev. B **47**, 1651 (1993).
 - [10] Y. Takimoto, F. D. Vila, and J. J. Rehr, J. Chem. Phys. **127**, 154114 (2007).
 - [11] J. Crank and P. Nicholson, Proc. Cambridge Philos. Soc. **43**, 50 (1947).
 - [12] C. Attaccalite, M. Grüning, and A. Marini, Phys. Rev. B **84**, 245110 (2011).

Exciton-driven giant non-linear overtone signals from buckled hexagonal monolayer GaAs

Himani Mishra and Sitangshu Bhattacharya*

*Nanoscale Electro-Thermal Laboratory, Department of Electronics and Communication Engineering,
Indian Institute of Information Technology-Allahabad, Uttar Pradesh 211015, India*

We report here a giant $|\chi_{baa}^2| = 780$ pm/V second harmonic and $|\chi_{aaa}^3| = 1.4 \times 10^{-17}$ m²/V² third harmonic signal from single atomic sheet of buckled hexagonal GaAs. We demonstrate this through the solution of an ab-initio real-time Bethe-Salpeter equation by including the electron-hole screened-exchange self-energy. The coupling between time-dependent external electric field and correlated electrons is treated within the modern theory of polarization. The result of our calculation envisage monolayer GaAs to be a prominent member in the material library of non-linear signal generations.

Breaking and pairing of symmetry rules in crystalline structure leads to many exciting physical phenomena. For example, the pairing of a broken-inversion and time-reversal symmetry in presence of a laser constructs a direct valley entangled electron-hole recombination that sparks a strong linear (i.e., absorption) as well as a non-linear optical (NLO) response (i.e., second, third, and other higher harmonic generations). In recent years, there had been benchmark spectroscopic experiments performed on exfoliated and van der waals epitaxy monolayer (ML) of transitional metal dichalcogenides (TMDCs) [1–7] and monochalcogenides (TMMCs) [8, 9] demonstrating extraordinary NLO responses. These materials possess a crystalline non-centro-symmetry and therefore, the non-cancellation of induced dipole leads to the second harmonic generation (SHG) as a lowest detected NL response. Such responses find wide applications in two-dimensional (2D) optical modulators [10], surface morphology characterizations and sum and difference frequency generations [11, 12], etc.

The frequency dependent induced macroscopic polarization in an NL medium is governed by the infinite series representation in the Fourier transform plane [13, 14] $\varepsilon_0^{-1} \mathbf{P}_i(\omega) = [\chi_{ij}^{(1)}(\omega) \mathcal{E}_j(\omega) + \chi_{ijk}^{(2)}(-\omega; \omega_1, \omega_2) \mathcal{E}_j(\omega_1) \mathcal{E}_k(\omega_2) + \chi_{ijkl}^{(3)}(-\omega; \omega_1, \omega_2, \omega_3) \mathcal{E}_j(\omega_1) \mathcal{E}_k(\omega_2) \mathcal{E}_l(\omega_3) + \dots]$ where $\chi_{ij}^{(1)}$ is the linear response, $\chi_{ijk}^{(2)}$ is the SHG response, $\chi_{ijkl}^{(3)}$ is the third harmonic generation (THG) response and so on, and $\mathcal{E}(t)$ is the time-dependent (TD) external electric field. SHG is the condition when $\omega_1 = \omega_2 = \omega$, thus $\chi_{ijk}^{(2)}(-2\omega; \omega, \omega)$. THG is the condition when $\omega_1 = \omega_2 = \omega_3 = \omega$, thus $\chi_{ijkl}^{(3)}(-3\omega; \omega, \omega, \omega)$. The index i is the polarization direction while j, k, l, \dots are the electric field directions.

Within the linear response theory, $\Im \chi_{ij}^{(1)}(\omega)$ defines the absorption spectra characterized by excited electron-hole pairs. Often, these excited pairs, called as excitons live a longer life by circling each other about their common center of mass bounded by a Coulombic attraction. In atomically thin sheet with weak screening, this pairing is equivalent to a 2D hydrogen-like atom with quantized energy levels. The landscapes of these excitons can be obtained as peaks in the photo-luminescence spectroscopy with similar distinct optical spectrum, and therefore

the luminosity in these materials can be tailored via tuning their exciton properties, notably their energies and ultra-fast lifetimes.

The SHG response $|\chi_{ijk}^{(2)}(-2\omega; \omega, \omega)|$, in principle is obtained from the experimental intensity counts and consequently calculated with physics-based models formulated at the level of “bulk” and “sheet” approximations [15]. These two models are related by a scaling factor F [16], along with the linear refractive index of ML (at ω and 2ω) and deposited substrate (at ω). This combined pre-factor essentially provides a 3-4 orders of magnitude difference between the two models. For instance, the 2D exfoliated MoS₂ [15] and van der waals epitaxy GaSe [8] reportedly exhibits an extremely large SHG signal of the order 10^5 and 10^3 pm/V respectively when calculated using the bulk model. Unlikely, this sheet model predicts only upto ~ 100 -500 and ~ 400 pm/V respectively [15].

The THG $|\chi_{ijkl}^{(3)}(-3\omega; \omega, \omega, \omega)|$ is likewise indirectly evaluated by measuring the average power of the TH beam and using an approximated bulk model. The reported THG response for 2D MoS₂ and WSe₂ is found to be in the order of 10^{-19} m²V⁻² [2, 7]. As far as we know, in ML family, the best THG response is from graphene and is in the order of 10^{-16} m²V⁻² [17, 18]. However, graphene is centro-symmetric and thus the SHG is identically zero.

First-principles calculations based on the solution of the many-body GW and Bethe-Salpeter equation (BSE) [19, 20] are nowadays the most reliable theoretical approach to investigate exciton affairs in crystals. While their high computational cost prevents their application to large defective systems, it has been undoubtedly proven that ab-initio GW+BSE calculations are the necessary tool to obtain fundamental understanding and guide new experiments on bulk and low-dimensional materials [21]. The excitons spectra within the linear optics can be achieved by the solution of a static BSE, whereas it needs the solution of a TD-BSE to efficiently understand the NL behaviour [22]. In-fact, the reduced SHG values mentioned in the preceding paragraph are also supported by the ab-initio calculations [23], thus validating the sheet model to be a more accurate description for SHG in MLs. Using the first principles based calculations and a real-time (RT) approach [24] to solve TD-BSE, we estimate the SHG and THG responses in ML buckled GaAs. We report in this letter that ML GaAs offers a giant exciton binding energy of 1.10 eV, an SHG of 780 pm/V and a THG of 1.4×10^{-17} m²V⁻². These appealing all-in-one values reinforce the entry of ML GaAs as a

* Corresponding Author's Email: sitangshu@iiita.ac.in

prominent member in the NL opto-electronics family.

To support our results, we start with the ground state

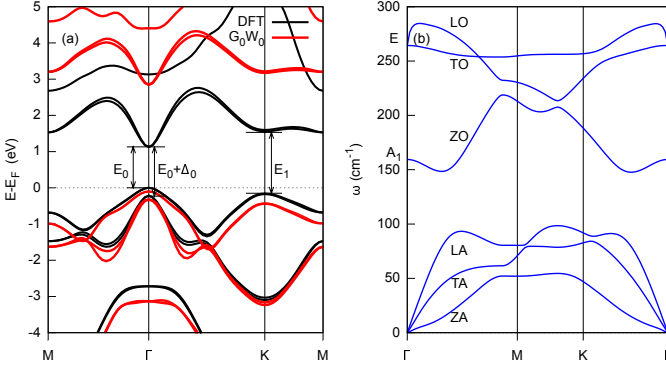


FIG. 1. (a) Electronic dispersion of ML buckled GaAs in accordance to ground state DFT and excited state G_0W_0 theory. The zero-level is set at the top of the DFT valence band in which E_F is the Fermi energy. The single-shot GW or G_0W_0 improves the gap E_0 at Γ by 1.82 eV. The valence spin-splitting is 0.22 eV. E_1 is the gap at \mathbf{K} . (b) Phonon dispersion showing no soft modes at Γ . A_1 and E modes are both infra-red and Raman active and there is no LO-TO splitting.

calculations (For a detailed methodology, see [25].) as shown in Fig. 1. The convergence criteria are demonstrated in the supplemental section [26]. ML buckled GaAs bears the same hexagonal in-plane lattice symmetry as in graphene [27]. Here we note that, the most favourable bonding structure for group III elements is sp^2 hybridization which results in a trigonal planar structure. Unlikely, due to higher ionic radius in group V elements, P, As and Sb prefers trigonal pyramidal structure with sp^3 bonding. Therefore, a stable ML GaAs is expected to showcase a mixture of sp^2 - sp^3 hybridization which results in a prominent buckling [27]. We verified the ML GaAs thermodynamic stability by the phonon dispersion, which portrays no soft-modes in the lower frequency branches. At Γ of the Brillouin zone (BZ), all the optical out-of-plane ZO (159 cm^{-1}), and the degenerate in-plane longitudinal (LO) and transverse (TO) modes (264 cm^{-1}) are infra-red as well as Raman active. From our spinor calculations [26] we find that at Γ , the orbital weightage of lowest conduction band and spin-splitting top two valence bands are due to the occupancy of Ga $4S_{1/2}$ (spin quantum number $m_s = +1/2$), As $4P_{3/2}$ ($m_s = +1/2$) and As $4P_{1/2}$ ($m_s = -1/2$) respectively. Apparently, the valence spin-orbit splitting (Δ_0) and the direct band-gap (E_0) at Γ is 0.22 and 1.13 eV respectively.

For the excited state calculations, a G_0W_0 formalism [22, 28] is used which resulted in a self-energy (sum of Hartree-Fock and dynamic) correction of 1.82 eV to E_0 leading to a gap of 2.95 eV (See Fig. 1(a)). For a detailed methodology, see [29]). The corresponding valence spin-orbit splitting improvements are insignificant. The absorption spectra is obtained by solving a coupled electron-hole Green's propagator with screen-exchange (SEX) potential in the self-energy correction (See the supplemental section [26] for a theoretical discussion on GW and BSE). The quasi-particle energy corrections were borrowed from the preceding G_0W_0 calculations. In both G_0W_0 and BSE computations, a necessary Coulomb truncation was applied along the out of plane direction. The screening part W_0 is obtained by solving a statically

(dynamically for G_0W_0) screened microscopic dielectric function evaluated at the level of random phase approximation which also included the local field effects. The full diagonalization of the BS matrix is finally implemented after considering the anti-resonant elements as well (i.e., beyond the Tamm-Dancoff approximation [30]). The spectra in Fig. 2 demonstrates three relevant peaks in the energy range of 1.8-2.5 eV. These peaks correspond to three inter-band critical points (CPs) [31] E_0 , $E_0 + \Delta_0$ and E_1 (See Fig. 1(a) here) with exciton peak positions at 1.85 eV, 2.07 eV and 2.32 eV respectively. E_0 and E_1 CPs are due to transition from highest valence band to the lowest conduction band at Γ and \mathbf{K} points of the BZ respectively. $E_0 + \Delta_0$ corresponds to transition from next highest valence band to the lowest conduction band at Γ . The first two excitonic peaks are due to the spin-splitting of the valence band in which we see that the peak position difference is exactly Δ_0 in the electronic dispersion. From the exciton peak positions, we measure a binding energy of 1.10 eV for the lowest exciton. This first peak E_0 is formed by a pair of degenerate dark and bright exciton. The information on dark or bright flavour is dependent on the spin selections in the bands where transitions occur. We find here that intra-valley transitions with

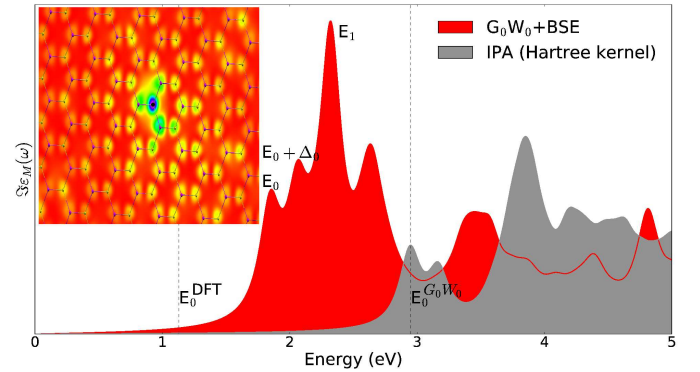


FIG. 2. Absorption spectra (i.e., the imaginary part of the macroscopic dielectric function $\epsilon_M(\omega)$) as function of photon energy using $G_0W_0 + \text{BSE}$ and IPA (Hartree-kernel) energy corrections. The dotted lines are the DFT and G_0W_0 gap energies at 1.13 and 2.95 eV respectively. The inset shows exciton wavefunction unfolded over the ML GaAs real space lattice. The hole is situated on the top of As atom at a distance of 1 Å and is shown by a dark spot. The exciton wave-function extends to one unit cell which makes the same to be a Frenkel-type.

anti-parallel spins produce bright excitons and vice versa. This showcases that the excitons forming from $E_0 + \Delta_0$ as well as E_1 (the bottom conduction and top degenerate valence band at \mathbf{K} is formed by Ga $4S_{1/2}$, $m_s = +1/2$ electrons and As $4P_{1/2}$, $m_s = +1/2$ respectively) transitions are both bright and non-degenerate. In the non-interacting picture (independent particle approximation, IPA) upto the level of Hartree kernel, the absorption spectra blue-shifts entirely with reduced peak amplitudes and broadened valleys. Interestingly, the E_0 exciton wavefunction unfolds over the real space ML lattice with a radius of approximately 16 Å (\sim four unit cells), which characterises it to be a Frenkel exciton.

In order to capture the NL responses, we solve in real-time the time-dependent Schrödinger equation, in presence of an external $\mathcal{E}(t)$. The induced macroscopic polarization for extended systems is calculated using King-Smith and

Vanderbilt formalism [32] which uses a Berry's geometric phase of the momentum state \mathbf{k} (See the supplemental section [26] for a theoretical discussion on NL responses). Buckled ML GaAs possess a C_{2v} - $\bar{3}m$ symmorphic group. The symmetry group arguments leads to non-vanishing susceptibility tensor elements [14] $\chi_{bbb}^{(2)} = -\chi_{baa}^{(2)} = -\chi_{aab}^{(2)} = -\chi_{aba}^{(2)}$ in which a and b are the in-plane ML axes. In order to verify first that the time dependent Schrödinger equation with SEX kernel in the system Hamiltonian (i.e., the TD-BSE) converge to a time independent excitonic BSE at weak intensities, we hit our ML system with a delta-like electric field at low intensity of 500 KWcm^{-2} . An *a-priori* Hartree and SEX collision integrals were carried out with an energy cut-off of 35 Ry to evaluate the Hartree+SEX self-consistent potentials. We note here that one can also calculate such potentials at each step in the dynamics, for which the results are same. The equation of motion (EOM) is integrated using a Crank-Nicholson algorithm [33] at a time-step of 10 as. The application of a delta-like

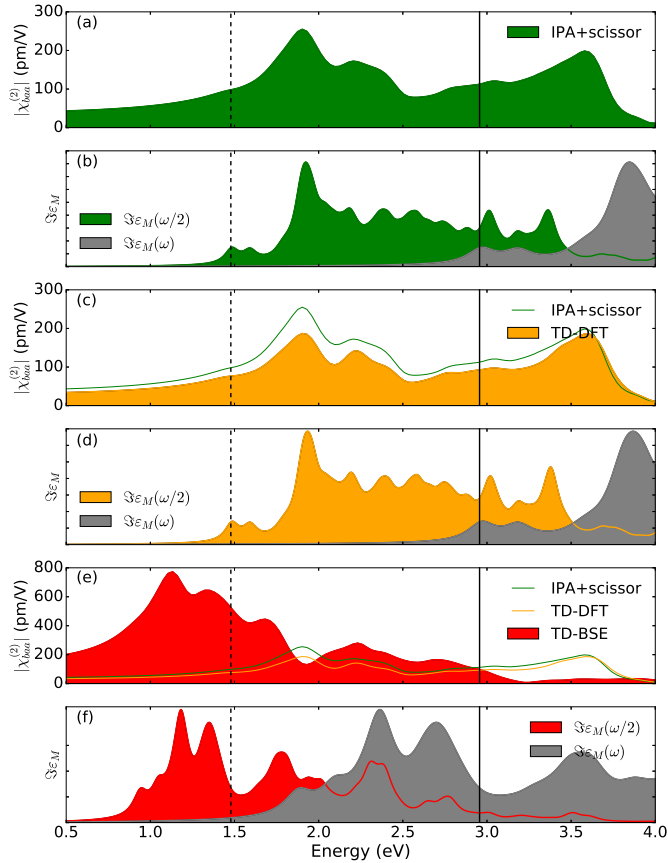


FIG. 3. Non linear SHG spectra of ML buckled GaAs as function of laser frequencies. (a), (c) and (e) are the SHG computed using IPA+scissor, TD-DFT and TD-BSE level of theory respectively. (b), (d) and (f) shows the absorption spectra computed at ω and $\omega/2$ under the IPA+scissor, TD-DFT and TD-BSE level of theory respectively. The solid and dashed vertical lines are for the ω and $\omega/2$ gaps.

impulse probes the system response at all frequencies. The linear $\chi_{ij}^{(1)}$ is *a-posteriori* calculation and we found to be in excellent agreement to the response obtained directly by solving the time-independent BSE (See Fig. S10(a) in the supplemental section [26]). It should be noted that a sudden switching-on of the external field sparks spurious initial non-linearities in the macroscopic

polarization function, which should be filtered out (See Fig. S10(c) in the supplemental section [26]). For this, a finite dephasing time of about 7 fs is added in the EOM Hamiltonian amounting to a damping of 0.2 eV. This phenomenological damping [24] also mimic the presence of any experimental dissipative effects like electron scatterings, defects and lattice vibrations. We run this simulation for 55 fs. We carefully note that beyond the dephasing time of about 32 fs (almost 5 dephasing time constants), all the spurious components in the polarization are exponentially diminished. The extraction of the responses are evaluated in this time window between 32 fs to 55 fs.

Based on the preceding method, we now demonstrate the SHG response using a quasi-sinoidal monochromatic field for three hierarchical perturbed Hamiltonian models in the EOM namely, TD-IPA, TD-DFT and TD-BSE (See Eqns. (21)-(24) in the Supplementary Section [26]). The external field is along a -axis while the SHG is measured along b -axis. Figure 3(a) exhibits the response for IPA. To this IPA and for all subsequent discussions, a rigid shift in the gap has been deployed by a scissor operator instead of the G_0W_0 correction. A scissor correction is sufficient in this case as we target to achieve the information of one, two or three photon absorption processes that influence the response spectra. These processes in SHG is extracted by comparing with $\Im\chi_{ij}^{(1)}(\omega)$ and $\Im\chi_{ij}^{(1)}(\omega/2)$, at the same Hamiltonian level as shown in Fig. 3(b). As $\Im\chi_{ij}^{(1)}$ are the linear responses, a delta-like field as mentioned in the preceding paragraph is then required for each of the case. The SHG IPA spectra is characterized by a number of peaks in the energy range 1.7-3.8 eV. The most prominent peak is at 1.91 eV. There exist also a small shoulder peak near 1.46 eV. When compared to $\Im\chi_{ij}^{(1)}(\omega/2)$, this shoulder peak is found due to the E_0 electronic transition at Γ and is a two-photon absorption process. The peak near 1.91 eV is due to the E_1 transition at \mathbf{K} and is also a two-photon processes. Apparently, the peak near 3.65 eV corresponding to a small hump in the $\Im\chi_{ij}^{(1)}(\omega)$, is mainly due to a one-photon process. The modifications in the NL and linear spectra in TD-DFT case (Figs. 3(c)-(d)) is due to the presence of time-dependent Hartree and exchange-correlation potentials respectively. Within the SEX kernel, the TD-BSE spectra modifies remarkably as shown in Fig. 3(e)-(f). This is due to the incorporation of exciton dynamics which is absent in the previous two cases. The shoulder peak as detected in IPA is now completely smeared out and the prominent peak at 1.16 eV emerges due to the E_1 transition. This is a two-photon process for which $|\chi_{baa}^{(2)}| = 780 \text{ pm/V}$ and almost five-times larger than the spectra of exfoliated ML MoS_2 when computed with the “sheet” model [15]. Similarly, the second and the third peaks are also a two-photon processes. Unlikely, the fourth peak is both due to one- and two-photon processes. In order to calculate the static response $\chi_{baa}^{(2)}(\omega = 0)$, one need to put a zero dephasing rate. However, this would mean an infinite simulation time and therefore data extrapolation is required. We extrapolate $|\chi_{baa}^{(2)}(\omega)|$ to obtain $|\chi_{baa}^{(2)}(\omega = 0)| = 150 \text{ pm/V}$.

In case of THG, we keep all the NL parameters same as in SHG, except the intensity which is increased to 10^6 KWcm^{-2} to achieve a significant response. The external

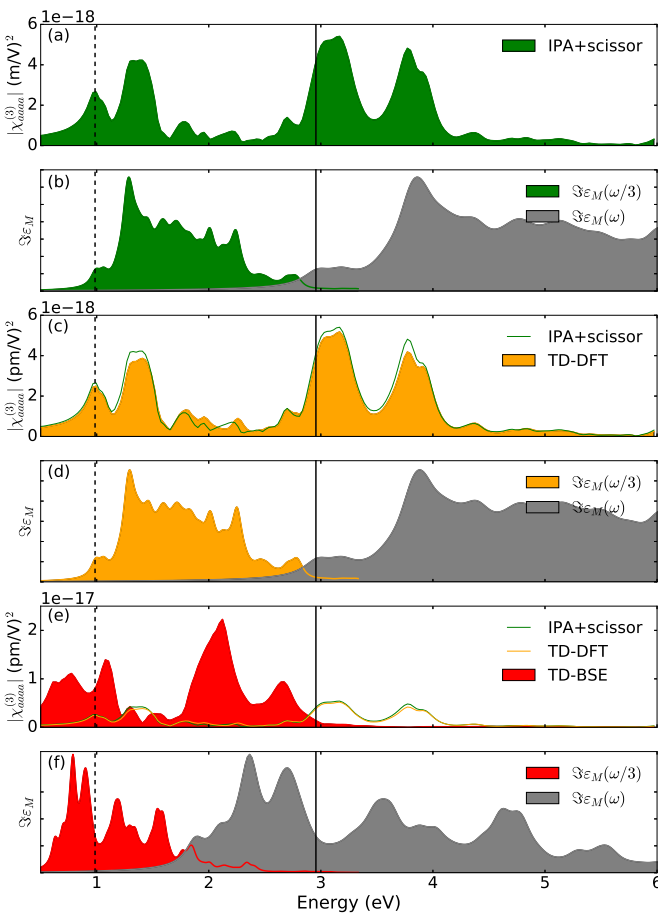


FIG. 4. Non linear THG spectra of ML buckled GaAs as function of laser frequencies. (a), (c) and (e) are the THG computed using IPA+scissor, TD-DFT and TD-BSE level of theory respectively. (b), (d) and (f) shows the absorption spectra computed at ω and $\omega/3$ under the IPA+scissor, TD-DFT and TD-BSE level of theory respectively. The solid and dashed vertical lines are for the ω and $\omega/3$ gaps.

field is along a -axis and thus we look for $|\chi_{aaaa}^{(3)}(\omega)|$. In a similar approach to SHG, we start with IPA as shown in Fig. 4(a) and compare the respective spectra with $\Im\chi_{ij}^{(1)}(\omega)$ and $\Im\chi_{ij}^{(1)}(\omega/3)$ in Fig. 4(b). The first peak is in the transparency region at 0.98 eV, is due to the E_0 transition and is a three-photon absorption process.

The most prominent peak at 3.16 eV is due to $E_0+\Delta_0$ transition and is a one-photon process. The on-set of this peak near 2.81 eV is however due to both one- and three-photon processes. Similar to SHG, the THG response variations in TD-DFT (Fig. 4(c) and (d)) is because of time-dependent Hartree and exchange-correlation potentials respectively. However, the SEX kernel modifies the response in Fig. 4(e) remarkably. Red-shifted peaks in the transparency region at 0.62 and 0.69 eV emerge due spin-splitted E_0 and $E_0+\Delta$ transitions respectively (in-fact the difference when multiplied by 3 gives Δ) and is a three-photon process. Likewise, peak at 0.78 eV is again a three-photon process due to E_1 transition. The peak near 1.08 eV is the most prominent three-photon process in the same region and emerges due to a broadened shoulder peak around the same energy as shown in Fig. 4(f). At this energy, we note the $|\chi_{aaaa}^3|=1.4\times 10^{-17}$ m²/V². This is in two order magnitude larger than reportedly exfoliated ML MoS₂ and WSe₂[2, 7]. The next two consecutive humps are again a three-photon process. The giant peak at 2.13 eV is a one-photon process and is due to the E_1 transition. The on-set of this peak near 1.76 eV is due to both one- and three-photon processes. We note here that in all our NL computations, the peak electric field is of the order 10^7 Vm⁻¹. Such values are in-fact weak enough to initiate a Zener breakdown.

To summarise, we use the first principles many-body approach and evaluate both linear as well as non-linear responses in buckled ML GaAs. We go beyond the static theory of the BSE to evaluate the non-linear optical harmonic generations. The inclusion of exciton dynamics significantly enhances both the SHG and THG responses compared to ML TMDCs and TMMCs. The prominent SHG and THG responses are due to the two- and three-photon absorption processes and falls in the transparency region respectively. These giant responses open the possibility to efficiently use buckled ML GaAs in an already established process technology foundry for the generation of non-linear signals.

ACKNOWLEDGMENTS

Both the authors acknowledge the computational support from Institute's Central Computational Facility, CCF. HM acknowledges MHRD, Govt. of India, for providing fellowship.

-
- [1] N. Kumar, S. Najmaei, Q. Cui, F. Ceballos, P. M. Ajayan, J. Lou, and H. Zhao, Phys. Rev. B **87**, 161403 (2013).
 - [2] R. Wang, H.-C. Chien, J. Kumar, N. Kumar, H.-Y. Chiu, and H. Zhao, Appl. Mater. Interfaces **6**, 314 (2014).
 - [3] G. Wang, X. Marie, I. Gerber, T. Amand, D. Lagarde, L. Bouet, M. Vidal, A. Balocchi, and B. Urbaszek, Phys. Rev. Lett. **114**, 097403 (2015).
 - [4] Y. Li, Y. Rao, K. F. Mak, Y. You, S. Wang, C. R. Dean, and T. F. Heinz, Nano Lett. **13**, 3329 (2013).
 - [5] L. M. Malard, T. V. Alencar, A. P. M. Barboza, K. F. Mak, and A. M. de Paula, Phys. Rev. B **87**, 201401 (2015).
 - [6] J. Ribeiro-Soares, C. Janisch, Z. Liu, A. L. Elias, M. S. Dresselhaus, M. Terrones, L. G. Cançado, and A. Jorio, 2D Mater. **2**, 045015 (2015).
 - [7] H. G. Rosa, H. Y. Wei, I. Verzhbitskiy, M. J. F. L. Rodrigues, T. Taniguchi, K. Watanabe, G. Eda, V. M. Pereira, and J. C. V. Gomes, arXiv:1803.01647 (2018).
 - [8] X. Zhou, J. Cheng, Y. Zhou, T. Cao, H. Hong, Z. Liao, S. Wu, H. Peng, K. Liu, and D. Yu, J. Am. Chem. Soc. **137**, 7994 (2015).
 - [9] J. Zhou, J. Shi, Q. Zeng, Y. Chen, L. Niu, F. Liu, T. Yu, K. Suenaga, X. Liu, and J. Lin, 2D Mater. **5**, 025019 (2018).
 - [10] Z. Sun, A. Martinez, and F. Wang, Nat. Photon. **10**, 227 (2016).
 - [11] Y. R. Shen, Nature **337**, 519 (1989).
 - [12] D. Smirnova, S. Kruk, D. Leykam, E. M.-G. D.-Y. Choi, and Y. Kivshar, Physical Rev. Lett. **123**, 103901 (2019).

- [13] P. A. Franken, A. E. Hill, C. W. Peters, and G. Weinreich, *Phys. Rev. Lett.* **7**, 118 (1961).
- [14] R. W. Boyd, *Non Linear Optics*, 3rd ed. (Academic Press, New York, United States of America, 2008).
- [15] D. J. Clark, V. Senthikumar, C. T. Le, D. L. Weerawarne, B. Shim, J. I. Jang, J. H. Shim, J. Cho, Y. Sim, M.-J. Seong, S. H. Rhim, A. J. Freeman, K.-H. Chung, and Y. S. Kim, *Phys. Rev. B* **90**, 121409 (2014).
- [16] $\chi_{bulk}^{(2)} = 32\pi F \frac{n_{2D}(\omega)\sqrt{n_{2D}(2\omega)}}{(n_{substrate}+1)^3} \chi_{sheet}^{(2)}$, in which n is the refractive index [15]. F is in the order of 10 and signifies a “scaling factor” that takes care of the reflectance and transmittance emerging due to the refractive index mismatches between the bulk crystal and the underlying substrate and air, respectively. This combined prefactor is close to 10^3 which scales $|\chi_{bulk}^{(2)}|$ to be in the range 10^5 .
- [17] A. Säynätjoki, L. Karvonen, J. Riikonen, W. Kim, S. Mehravar, R. A. Norwood, N. Peyghambarian, H. Lipsanen, and K. Kieu, *ACS Nano* **10**, 8441 (2013).
- [18] S.-Y. Hong, J. I. Dadap, N. Petrone, P.-C. Yeh, J. Hone, and R. M. O. Jr., *Phys. Rev. X* **3**, 021014 (2013).
- [19] G. Onida, L. Reining, and A. Rubio, *Rev. Mod. Phys.* **74**, 601 (2002).
- [20] F. Paleari, H. P. Miranda, A. Molina-Sánchez, and L. Wirtz, *Phys. Rev. Lett.* **122**, 187401 (2019).
- [21] Z. Ye, T. Cao, K. O'Brien, H. Zhu, X. Yin, Y. Wang, S. G. Louie, and X. Zhang, *Nature* **513**, 214 (2014).
- [22] C. Attaccalite and M. Grüning, *Phys. Rev. B* **88**, 235113 (2013).
- [23] C. Attaccalite, M. Palummo, E. Cannuccia, and M. Grüning, *Phys. Rev. Mat.* **3**, 074003 (2019).
- [24] C. Attaccalite, M. Grüning, and A. Marini, *Phys. Rev. B* **84**, 245110 (2011).
- [25] All density functional theory (DFT) calculations were carried out with Quantum Espresso package [34]. A fully relativistic, norm-conserving pseudopotential with PBE exchange-correlational functional was generated [35]. The 3d semi-core orbital was included in both Ga and As along with 4s and 4p valence electrons. A kinetic cut-off energy of 120 Ry [26] was selected. The BZ was sampled on a $12 \times 12 \times 1$ grid using a Γ centred Monkhorst-Pack scheme with the force and energy thresholds of 10^{-5} Ry/Bohr and 10^{-5} Ry respectively. A vacuum of 30 Å in either side of the ML was selected to prevent the Coulombic interference between the repeated images. A two-spinor wave-function along with the non-collinear and spin-orbit coupling criteria was expanded in the plane-wave basis set. The resulted in-plane and buckled lattice constants are $a=4.05$ Å and 0.58 Å respectively. The lattice vibration calculations was carried out on a uniform $18 \times 18 \times 1$ dense phonon grid using a rigid self-consistent error threshold below 10^{-18} Ry.
- [26] See Supplemental Material at <http://link.aps.org/supplemental/> for details of theory and convergence criteria.
- [27] H. L. Zhuang, A. K. Singh, and R. G. Hennig, *Phys. Rev. B* **87**, 165415 (2013).
- [28] D. Sangalli, A. Ferretti, H. Miranda, C. Attaccalite, I. Marri, E. Cannuccia, P. Melo, M. Marsili, F. Paleari, A. Marrazzo, G. Prandini, P. Bonfà, M. O. Atambo, F. Affinito, M. Palummo, A. Molina-Sánchez, C. Hogan, M. Grüning, D. Varsano, and A. Marini, *J. Phys.: Condens. Matter* **31**, 325902 (2019).
- [29] The linear and NL excitations were computed using the extended version of the many-body perturbation theory YAMBO package [22, 28]. A Godby-Needs [36] plasmon-pole approximate model was used to calculate the microscopic dynamic dielectric screening function. 200 bands (28 occupied and 172 unoccupied) along with a response block size of 7 Ry were considered in the evaluation of local-field effects within the random-phase approximation. The transferred momentum \mathbf{q} divergences were fixed using a random integration method [37, 38] in which by keeping the potential unchanged, a smooth momenta integrand function is assumed in each small volumetric region of the BZ. This BZ integral is finally evaluated through a Monte Carlo method. 10^6 random- \mathbf{q} points with a cut-off of 3 Ry were found sufficient to cover and compute the BZ integral fully. Likewise in DFT, a Coulomb truncation of 30 Å on either ML side in form of a box structure was used. The BSE computation was done by dense sampling the BZ to $72 \times 72 \times 1$ on a shifted grid and then mapped to the $12 \times 12 \times 1$ regular grid. This methodology [39] essentially speed up the numerical computation without losing the numerical accuracy. The linear spectra is found to get converged with top five valence and lowest five conduction bands. To know the exciton wave-function raduis, a hole was kept on the top of As atom at a distance of 1 Å. In NL calculations, a proper choice of gauge, i.e., the length-gauge was used instead of velocity-gauge, as the later suffers numerical divergences in the response functions at low frequencies [22]. The subsequent calculations (as described in the main text) were then carried out with the same $72 \times 72 \times 1$ grid and same number of transition bands.
- [30] M. Grüning, A. Marini, and X. Gonze, *Nano Lett.* **9**, 2820 (2009).
- [31] P. Lautenschlager, M. Garriga, S. Logothetidis, and M. Cardona, *Phys. Rev. B* **35**, 9174 (1987).
- [32] R. D. King-Smith and D. Vanderbilt, *Phys. Rev. B* **47**, 1651 (1993).
- [33] J. Crank and P. Nicholson, *Proc. Cambridge Philos. Soc.* **43**, 50 (1947).
- [34] P. Giannozzi, O. Andreussi, T. Brumme, O. Bunau, M. B. Nardelli, M. Calandra, R. Car, C. Cavazzoni, D. Ceresoli, M. Cococcioni, N. Colonna, I. Carnimeo, A. D. Corso, S. de Gironcoli, P. Delugas, R. A. DiStasio Jr, A. Ferretti, A. Floris, G. Fratesi, G. Fugallo, R. Gebauer, U. Gerstmann, F. Giustino, T. Gorni, J. Jia, M. Kawamura, H.-Y. Ko, A. Kokalj, E. Küçükbenli, M. Lazzeri, M. Marsili, N. Marzari, F. Mauri, N. L. Nguyen, H.-V. Nguyen, A. O. de-la Roza, L. Paulatto, S. Poncé, D. Rocca, R. Sabatini, B. Santra, M. Schlipf, A. P. Seitsonen, A. Smogunov, I. Timrov, T. Thonhauser, P. Umari, N. Vast, X. Wu, and S. Baroni, *J. Phys.: Condens. Matter* **29**, 465901 (2017).
- [35] D. R. Hamann, *Phys. Rev. B* **88**, 085117 (2013).
- [36] R. W. Godby and R. J. Needs, *Phys. Rev. Lett.* **62**, 1169 (1989).
- [37] O. Pulci, G. Onida, R. D. Sole, and L. Reining, *Phys. Rev. Lett.* **81**, 5374 (1998).
- [38] C. A. Rozzi, D. Varsano, A. Marini, E. K. U. Gross, and A. Rubio, *Phys. Rev. B* **73**, 205119 (2006).
- [39] D. Kammerlander, S. Botti, M. A. L. Marques, A. Marini, and C. Attaccalite, *Phys. Rev. B* **86**, 125203 (2012).